

# Structure-aware Completion of Photogrammetric Meshes in Urban Road Environment

Qing Zhu<sup>a</sup>, Qisen Shang<sup>a</sup>, Han Hu<sup>a,\*</sup>, Haojia Yu<sup>a</sup>, Ruofei Zhong<sup>b</sup>

<sup>a</sup>*Faculty of Geosciences and Environmental Engineering, Southwest Jiaotong University, Chengdu, China*

<sup>b</sup>*Beijing Advanced Innovation Center for Imaging Technology, Capital Normal University, Beijing, China*

---

## Abstract

Photogrammetric mesh models obtained from aerial oblique images have been widely used for urban reconstruction. However, photogrammetric meshes suffer from severe texture problems, particularly in typical road areas, owing to occlusion. This paper proposes a structure-aware completion approach to improve mesh quality by seamlessly removing undesired vehicles. Specifically, a discontinuous texture atlas is first integrated into a continuous screen space by rendering through a graphics pipeline. The rendering also records the necessary mapping for deintegration to the original texture atlas after editing. Vehicle regions are masked by a standard object detection approach, namely, Faster RCNN. Subsequently, the masked regions are completed, guided by the linear structures and regularities in the road region; this is implemented based on PatchMatch. Finally, the completed rendered image is deintegrated to the original texture atlas, and the triangles for the vehicles are also flattened so that improved meshes can be obtained. Experimental evaluation and analysis are conducted on three datasets, which were captured with different sensors and ground sample distances. The results demonstrate that the proposed method can produce quite realistic meshes after removing the vehicles. The structure-aware completion approach for road regions outperforms popular image completion methods, and an ablation study further confirms the effectiveness of the linear guidance. It should be noted that the proposed method can also handle tiled mesh models for large-scale scenes. Code and datasets are available at the project website<sup>1</sup>.

**Keywords:** Oblique Photogrammetry, 3D Model, Model Correction, Image Completion

---

## 1. Introduction

The demand for automatic modeling of city-scale urban environments has recently attracted increasing interest (Remondino et al., 2017). Specifically, high-quality 3D reconstruction of road networks, which form the skeleton of urban scenes, is useful in a variety of applications, including navigation maps, autonomous driving, and urban planning (Yang et al., 2017; Chen et al., 2019; Wenzel and Bulatov, 2019). Recently, massive airborne datasets have been collected for several cities around the world (Google, 2020; Sugarbaker et al., 2014; Isenburg, 2020). Although airborne light detection and ranging (LiDAR) has been widely used in the last two decades (Kada and McKinley, 2009; Haala and Kada, 2010), advances in large-scale structure-from-motion (SFM) (Schonberger and Frahm, 2016) and multi-view stereo (MVS) (Vu et al., 2009; Jancosek and Pajdla, 2011) pipelines have enabled the automatic generation of city-scale

---

\*Corresponding Author: han.hu@swjtu.edu.cn

<sup>1</sup><https://vrlab.org.cn/~hanhu/projects/mesh>

triangular surface models from aerial oblique images, which are also enriched with high-resolution textures.

Aerial oblique images are arguably the most widely used datasets for 3D modeling of urban environments (Google, 2020); however, photogrammetric point clouds and meshes are geometrically less accurate and regular than LiDAR points at similar resolutions (Nex and Gerke, 2014; Hu et al., 2016a). In addition, photogrammetric meshes are also commonly contaminated by occluded objects and topological defects (Verdie et al., 2015; Hu et al., 2016b), particularly in road areas. These issues require a practical approach to improve the quality of existing photo-realistic meshes from aerial oblique images. In particular, the major objective of this study is to remove vehicles from both the geometries and textures of mesh models so that clean results can be obtained for further applications. Despite the recent progress in the processing of textures of mesh models (Prada et al., 2018), MVS pipelines for photogrammetric meshes of road regions cause certain problems that should be addressed.

1) *Occlusion and dynamic objects.* Although penta-view aerial oblique camera systems can capture ground objects from multiple viewpoints (Remondino and Gerke, 2015), occlusions on the ground, particularly in road areas, are inevitable in urban environments with dense building rise-ups. The geometries of photogrammetric meshes are generally noise-laden, and the textures are severely blurred (Figure 1a). In addition, existing MVS pipelines cannot handle dynamic objects, *for example* vehicles. We argue that it is hardly possible to resolve these issues in an MVS pipeline for aerial oblique images because the aforementioned defects are inherently embedded in the images. Therefore, direct editing of the meshes to improve quality may be the most practical solution.

2) *Discrete and discontinuous atlases for textures.* A photogrammetric surface mesh, as a 2D manifold embedded in 3D space, should be unwrapped to 2D planar space so that it can be consumed by the textures. This step is also termed surface parametrization (Lévy et al., 2002). Although the existence of a continuous conformal map for any 2D manifold has been proved, in practice, photogrammetric meshes should be separated into different segments (*e.g.*, charts) and packed into one or multiple texture images (*e.g.*, atlases) (Figure 1b). Segmentation is generally used to alleviate distortion in surface parametrization for large patches and to achieve fitting into a single image with a limited field of view (Waechter et al., 2014). It is quite difficult to directly process texture images, which are discrete and discontinuous.

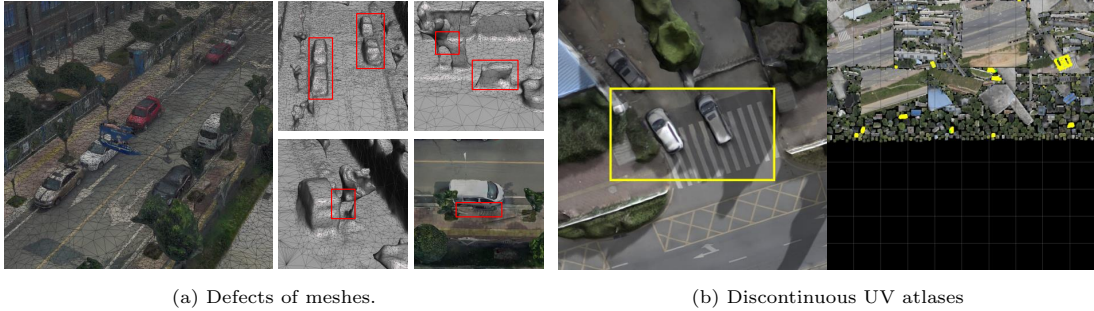


Figure 1: Common problems of photogrammetric meshes.

To resolve these issues, we propose a structure-aware completion method for the textures of photogrammetric meshes to improve the mesh quality of urban roads. The intuitive principle is to detect vehicles, directly flatten the geometries, and replace the textures according to repeated patterns of urban roads. Specifically, we first transform the discrete texture atlas to a continuous screen space through the graphics pipeline. Subsequently, vehicles are detected and masked

as voids using publicly available deep learning approaches [Ren et al. \(2015\)](#). Then, the void areas are automatically completed using the proposed structure-aware image completion method. Finally, the completed textures are remapped to the original texture atlases, and the triangles corresponding to the voids are flattened.

In summary, the major advantages of the proposed mesh correction approaches are the following: 1) an efficient strategy to handle discontinuous texture atlases by directly rendering photogrammetric meshes, and 2) structure-aware image completion methods to remove vehicles on the roads of urban environments. The rest of this paper is organized as follows: Section 2 provides a brief review of related work. Section 3.1 introduces the mesh completion workflow. Sections 3.2, 3.3, and 3.5 elaborate the details of proposed method. Experimental evaluations are presented in Section 4. Finally, the last section concludes the paper.

## 2. Related work

The most relevant literature includes 1) texture mapping and processing ([Waechter et al., 2014](#); [Prada et al., 2018](#)), 2) object detection ([Ren et al., 2015](#); [Redmon et al., 2016](#)), and 3) image completion ([He and Sun, 2012](#)).

1) *Texture mapping and processing.* Currently, massive collections of city-scale aerial oblique images ([Remondino and Gerke, 2015](#)) have been obtained. With the advances in bundle adjustment ([Hu et al., 2015](#); [Verykokou and Ioannidis, 2018](#)) and dense image matching ([Hirschmuller, 2008](#); [Hu et al., 2016a](#)) for aerial oblique images, high-density photogrammetric point clouds can be obtained, from which surface meshes can be constructed ([Kazhdan and Hoppe, 2013](#); [Jancosek and Pajdla, 2011](#)). These meshes are then enriched with high-resolution textures by mapping the color information from the original images ([Zhou and Koltun, 2014](#); [Bi et al., 2017](#); [Waechter et al., 2014](#)). In theory, any manifold surface immersed in 3D space can be continuously unwrapped in 2D space ([Crane et al., 2013](#)); this process is termed surface parametrization ([Lévy et al., 2002](#)). Unfortunately, however, a continuous parametrization inevitably leads to significantly distorted shapes in 2D space ([Sorkine et al., 2002](#)), particularly for large and irregular meshes. Therefore, the texture mapping of a photogrammetric mesh is intentionally segregated into different segments (*charts*), and different parts are then packed into a single or several texture images (*atlases*) ([Lévy et al., 2002](#); [Liu et al., 2019](#); [Limper et al., 2018](#)). The boundaries for different charts are commonly known as seam lines. Several similar strategies are available to generate seam lines or, equivalently, charts, including variational shape approximation ([Cohen-Steiner et al., 2004](#)), local geometries ([Allène et al., 2008](#); [Zhang et al., 2020](#)), and multi-view geometric and photometric consistencies ([Waechter et al., 2014](#); [Bi et al., 2017](#)).

The processing of discontinuous texture atlases is quite difficult ([Yuksel et al., 2019](#)). To alleviate color differences in the continuous image space (*i.e.*, image mosaicking), we could either estimate the color transfer function based on the overlapping region ([Yu et al., 2017](#); [Hu et al., 2019](#)), or reformulate the problem as a gradient-domain blending problem ([Agarwala, 2007](#); [Kazhdan et al., 2010](#)). However, in discontinuous texture atlases, it is difficult to detect or even define the overlaps and gradient breaks on the seam lines. Thus, [Waechter et al. \(2014\)](#) only locally blends the color in a region with a fixed width along seam lines. To resolve this discontinuity, [Prada et al. \(2018\)](#) and [Liu et al. \(2017\)](#) formulate the problem in a meticulously selected continuous function space based on the finite element approach. However, these approaches cannot handle varying mesh typologies and large texture sizes (e.g.,  $8192 \times 8192$ ) ([Waechter et al., 2014](#)), and therefore, they are probably not suitable for editing photogrammetric meshes. Instead, we propose a practical approach to edit mesh textures by efficiently generating a continuous mapping through orthogonal rendering of the meshes.

2) *Object detection.* Traditional object detection methods generally use low-level features, such as Harr-like features (Papageorgiou et al., 1998), local binary patterns (Ojala et al., 2002), and histograms of oriented gradients (Dalal and Triggs, 2005). Some notable approaches include the V-J detector (Viola and Jones, 2004) and deformable part models (Felzenszwalb et al., 2009). However, owing to the semantic gap between low-level vision features and high-level semantic information, only low performance has been achieved for a considerable time (Girshick et al., 2014). With the re-invention of deep neural networks, particularly deep convolutional neural networks, learned features (Simonyan and Zisserman, 2014) pre-trained on large datasets have demonstrated superior performance compared with previously known shallow methods. A typical approach, known as the regional convolutional neural network (RCNN) (Girshick et al., 2014), can perform unsupervised detection of the bounding boxes of certain salient objects (Uijlings et al., 2013), aggregate the features in the bounding box through regional pooling, and classify each bounding box into specified categories. This strategy is further improved by reusing the feature maps (Girshick, 2015) and learning the generation of bounding boxes (Ren et al., 2015); this strategy is known as Faster RCNN.

These approaches consist of two separate stages: detection and classification of bounding boxes. To improve efficiency, a more concise one-stage approach is proposed (Redmon et al., 2016), namely “you only look once.” Its principle is to tessellate an image into regular grids, and regress each grid to the corresponding locations and most likely classes. Similar approaches have been proposed to further improve effectiveness (Liu et al., 2016; Redmon and Farhadi, 2017, 2018). Owing to the superior performance of deep learning in object detection, we also use a standard approach (Ren et al., 2015) to detect vehicles on roads.

3) *Image completion.* With regard to filling void image regions, extensive research has been conducted on image inpainting and completion. The corresponding methods are based either on partial differential equations (PDEs) or on sampling.

Bertalmio et al. (2000) repaired images by diffusing the edge information of the region of interest (ROI) to unknown regions. A similar approach was proposed using total variation (Shen and Chan, 2002), and was improved through an anti-aliasing strategy (Aubert and Kornprobst, 2006). However, PDE-based methods cannot fill large voids, as they are only driven by local information.

Regarding sample-based approaches, Criminisi et al. (2004) selected the best matching patch according to the isophote. This method was improved by considering the weighted averaging of multiple patches (Wong and Orchard, 2008). A milestone on sample-based image completion is patch matching (Barnes et al., 2009), which significantly accelerates the search for the most similar patches through random guess and expansion. Several state-of-the-art methods are based on patch matching: He and Sun (2012) extracted transnational regularities using the statistics of patch offsets, and Huang et al. (2014) further considered affine deformations. Although sample-based methods can repair large missing images, they are limited to structured linear patterns (Iizuka et al., 2017), which are probably the most common patterns for urban roads.

Recently, image completion based on deep learning (Graves, 2013; Yeh et al., 2017; Iizuka et al., 2017) has made progress by using generative models (Iizuka et al., 2017; Yu et al., 2018; Nazeri et al., 2019). However, deep learning approaches rely on massive training data, which are difficult to obtain; otherwise, it is difficult to synthesize high-resolution images (Wu et al., 2017). In this paper, we propose a structure-aware image completion that directly uses linear features to guide the search for similar patches.



### 3. Structure-aware completion of photogrammetric meshes for urban roads

#### 3.1. Overview and problem setup

##### 3.1.1. Overview of the approach

To overcome the problem caused by discrete and discontinuous textures, we establish a one-to-one mapping between the atlas and the orthogonally rendered image, whereby vehicle regions are extracted and filled. In addition, we apply a linear feature, which is the most common feature in urban roads, to guide and constrain image completion and thus improve the output linear structures. The overall workflow of the proposed method is shown in Figure 2; it consists of five parts. Beginning with the textured meshes and an input ROI, we first render the geometry primitives (e.g., triangles) in the ROI to two buffers: an ID buffer that records the primitive IDs, and a color buffer that records the color information. Subsequently, we establish a mapping between a texel (a pixel in the texture atlas) and a pixel of color buffer using the corresponding primitive IDs. After texture integration, we apply Faster R-CNN to the integrated image to detect vehicles and generate a mask according to the bounding boxes of the detected objects. Subsequently, we complete the image with a mask using the proposed algorithm, which involves two sequential steps: detecting the road direction from translational regularities by RANSAC, and extracting edges from the road image. The proposed algorithm uses this information to guide and constrain the completion process. Finally, the completion result is used, and the pipeline is rendered to update the texture atlas so that automatic correction of the textured model can be achieved.

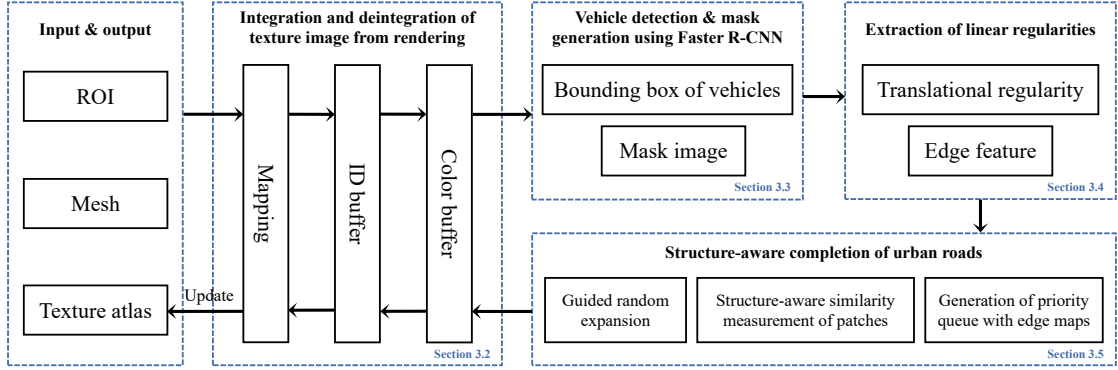


Figure 2: Workflow of photogrammetric mesh correction in road areas. First, the discontinuous texture of the selected ROI is integrated by rendering, vehicles are detected, and a mask image is generated using Faster R-CNN. Then, regularities are extracted and used to guide and constrain the image completion process. Subsequently, the corrected integrated image is deintegrated by rendering to obtain the corrected texture atlas. Finally, the texture atlas is replaced with a corrected texture atlas to achieve texture correction of the mesh.

##### 3.1.2. Problem setup

More formally, the inputs consist of a 2-manifold geometry mesh  $\mathcal{M}(V, F)$  and a 2D UV mesh  $\mathcal{M}'(V', F')$  (Prada et al., 2018), as shown in Figures 3 a and b.  $V \in \mathbb{R}^{3 \times N}$  and  $V' \in \mathbb{R}^{2 \times N'}$  are the vertices of the meshes. In general, the number of vertices is not equal to  $N \neq N'$  because of the seam lines in the mesh  $M$ .  $F \in \mathbb{Z}^{3 \times M}$  and  $F' \in \mathbb{Z}^{3 \times M'}$  are the facets; each column of  $F$  and  $F'$  records three indices into vertices  $V$  and  $V'$ , respectively. Although the indices may be different, the order and number of the facets recorded in  $F$  and  $F'$  are the same, that is,  $M = M'$ . There is also a texture image  $\mathcal{I}$  associated with the UV mesh  $\mathcal{M}'$ . To avoid confusion, we term the coordinates on the texture image *texel*  $\mathbf{t}(u, v)$  (Figure 3c) (Prada et al., 2018) rather than *pixel*  $\mathbf{p}(x, y)$  for normal images. The purpose of this study is to flatten the geometries by

modifying the vertices  $V$  of the mesh  $\mathcal{M}$ , and to correct the texture image  $\mathcal{I}$  so that cleaner street scenes can be obtained in an urban environment.

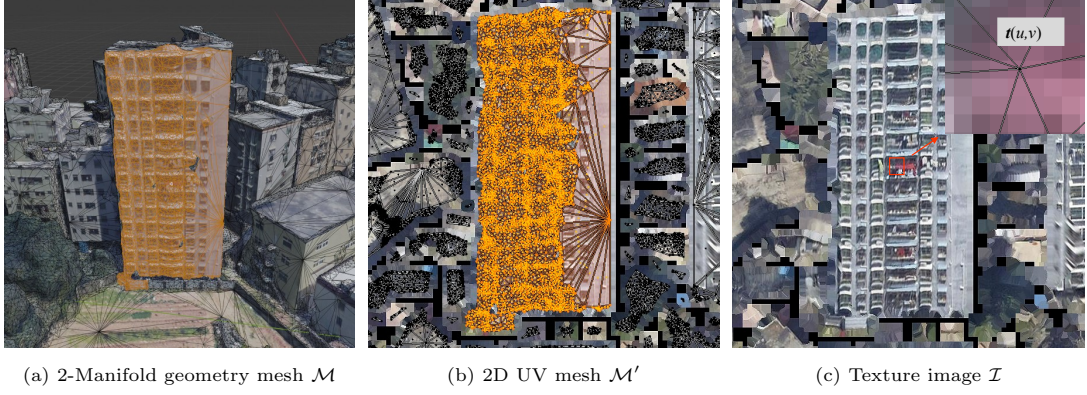


Figure 3: A textured mesh in this paper consists of three parts: a geometry mesh  $\mathcal{M}$ , an UV mesh  $\mathcal{M}'$ , and a texture image  $\mathcal{I}$ .

### 3.2. Integration and deintegration of texture image

As discontinuous texture images are difficult to process, we first integrate the texels in a specified ROI into a continuous image, by directly rendering the textured mesh models (Zhu et al., 2020a). After performing the correction steps in the continuous image space, we deintegrate the modified pixels to the corresponding texels using the methods described below. Figure 4 shows the integration and deintegration processes of the texture image.

#### 3.2.1. Texture integration

The graphics render pipeline can efficiently project the mesh models to the screen space, and shade the fragment on the screen from the texture. Despite the textured mesh models, two matrices are required that define the projection from the model space to screen viewport: the projection matrix  $\mathbf{P}$  and the view matrix  $\mathbf{V}$ . As in (Zhu et al., 2020a), we use the *ortho* and *perspective* routines in GLM (GLM, 2019) for the projection  $\mathbf{P}$  and view  $\mathbf{V}$  matrix, respectively. The parameters of the *ortho* and *perspective* routines can be intuitively determined through the bounding box of the mesh models in the selected ROI. In addition, the geometries outside the ROI are discarded in the following processing.

The direct output of the render pipeline is a color raster  $\mathcal{R}_c$ , which samples the texture by bilinear interpolation of the texels. However, if only  $\mathcal{R}_c$  is available, the information required to map between  $\mathcal{R}_c$  and the original texture image  $\mathcal{I}$  is insufficient. Therefore, we also allocate another raster  $\mathcal{R}_f$  in the render pipeline. Each pixel  $\mathbf{p}(x, y) \in \mathbb{Z}$  in  $\mathcal{R}_f$  stores the facet index  $f$  of the mesh  $F \in \mathcal{M}$  or, equivalently, the UV mesh  $F' \in \mathcal{M}'$ . It should be noted that  $\mathcal{R}_f$  and the color raster  $\mathcal{R}_c$  are obtained simultaneously in a single rendering frame. The *gl\_PrimitiveID* in the fragment language of OpenGL is a constant that contains the index of the current primitive in the rendering pipeline, that is,  $f = gl\_PrimitiveID$ . Similar inputs are also available for other graphic application programming interfaces. Therefore, both  $\mathcal{R}_c$  and  $\mathcal{R}_f$ , as shown in Figure 4, can be obtained in real time.

#### 3.2.2. Texture deintegration

To map the edited image  $\mathcal{R}_c$  back to the texture image  $\mathcal{I}$ , a one-to-one mapping should be established between the two images, that is,  $\mathbf{t} = T(\mathbf{p})$ , as shown in Figure 4. Although

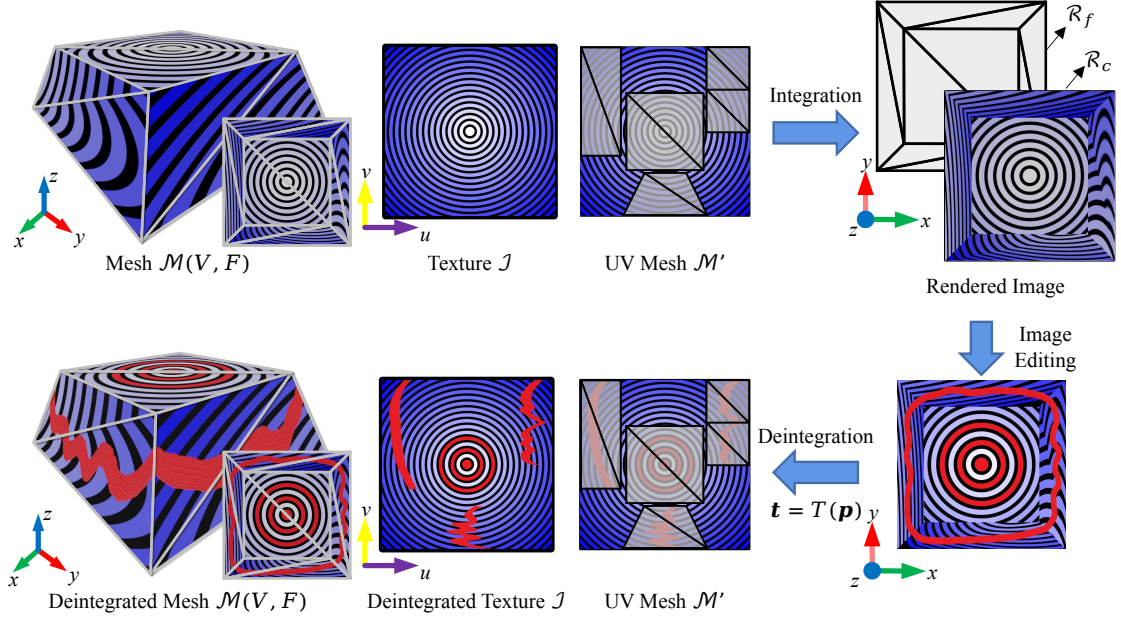


Figure 4: Integration and deintegration of texture image. Beginning with a mesh  $\mathcal{M}$ , a UV mesh  $\mathcal{M}'$ , and the texture  $\mathcal{I}$ , we first render the mesh in the ROI to two rasters: the color  $\mathcal{R}_c$  and the facet raster  $\mathcal{R}_f$ .  $\mathcal{R}_c$  and  $\mathcal{R}_f$  record the grayscale values and facet numbers from the original meshes, respectively. After editing  $\mathcal{R}_c$ , we estimate a mapping  $\mathbf{t} = T(\mathbf{p})$  using  $\mathcal{R}_f$  and deintegrating the edited pixels to the texture image.

the transformation from mesh  $\mathcal{M}$  to UV mesh  $\mathcal{M}'$  is generally assumed to be conformal (Lévy et al., 2002), we relax this assumption to an affine transformation because of numerical rounding or other factors. Therefore, we can use the trilinear coordinates  $\mathbf{c}(a, b, c)$  (Wolfram, 2020) to interpolate  $\eta(\cdot)$  the position inside the same facet  $f$  for the mesh  $\mathcal{M}$ , UV mesh  $\mathcal{M}'$ , and rendered image  $\mathcal{R}_c$ .

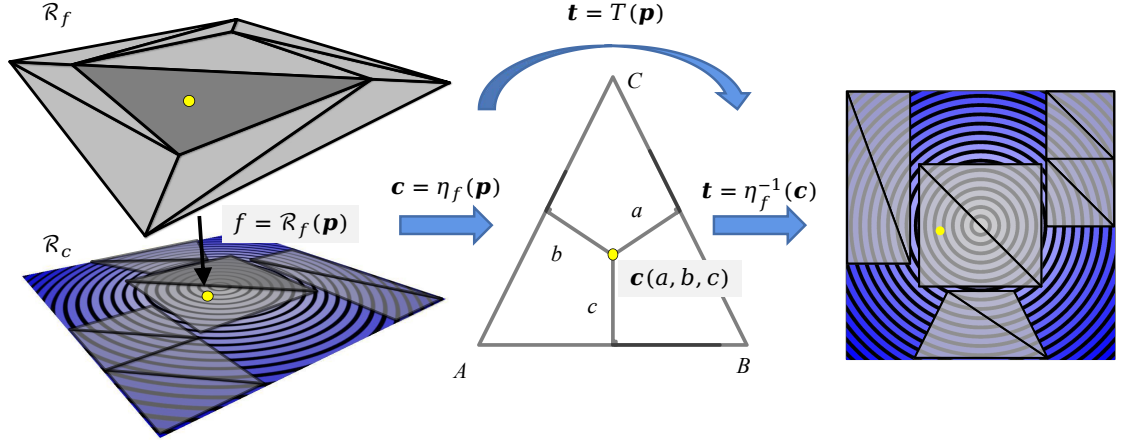


Figure 5: Mapping between rendered image  $\mathcal{R}_c$  and texture image  $\mathcal{I}$  using trilinear coordinates.

Figure 5 shows the process to establish the transformation  $\mathbf{t} = T(\mathbf{p})$ . For each modified pixel  $\mathbf{o} \in \mathcal{R}_c$ , the corresponding facet index is directly loaded from  $\mathcal{R}_f$  as  $f = \mathcal{R}_f(\mathbf{p})$ . The

trilinear coordinates of pixel  $\mathbf{p}$  inside the corresponding triangle  $f$  can be computed in closed form as  $\mathbf{c} = \eta_f(\mathbf{p})$  (Wolfram, 2020). Then, in the same facet of the UV mesh  $\mathcal{M}'$ , the inverse mapping directly yields the position of the texel as  $\mathbf{t} = \eta_f^{-1}(\mathbf{c})$ . In fact, inside each facet, the transformation  $\mathbf{t} = T(\mathbf{p})$  is equivalent to an affine transformation. In the implementation, the mapping  $T(\cdot)$  is pre-computed for each triangle and stored pixel-wise.

Another practical issue for the integration and deintegration processes is related to the data structure of the mesh models. The mesh models are tiled into small fragments and organized in a tree structure for different LODs. Each small tile is associated with a texture. In the implementation, the UV Mesh  $\mathcal{M}'$  also contains an array to store the atlas index. Moreover, multiple transformations  $T(\cdot)$  are used to account for multiple texture atlases. In fact, even without tiling, a single mesh can also contain multiple texture images; the same strategy is used to handle the above issue.

### 3.3. Vehicle detection and mask generation using Faster R-CNN

To remove the vehicles from the photogrammetric mesh models, we use Faster R-CNN (Ren et al., 2015) for vehicle detection in the rendered image  $\mathcal{R}_c$ , as shown in Figure 6. As Faster R-CNN (Ren et al., 2015) is a well-established and industrially proven method, we only briefly introduce the training process in the following.

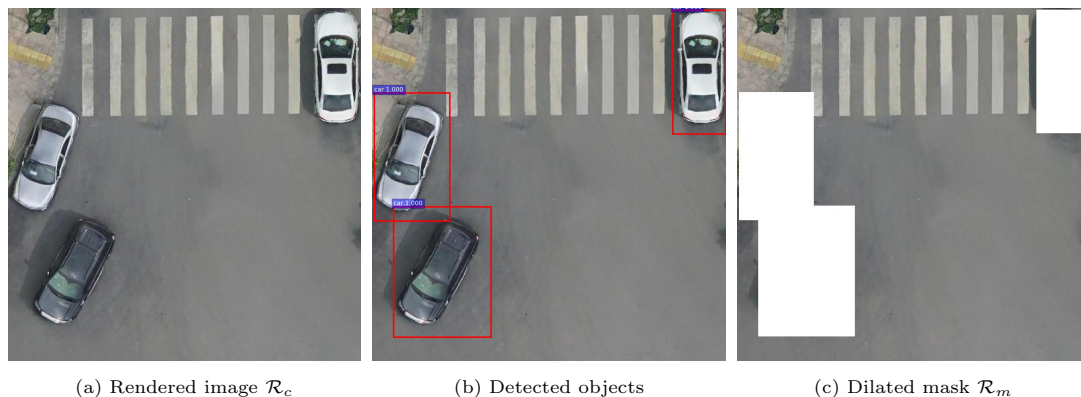


Figure 6: Vehicle detection and mask generation. Faster R-CNN is used to detect objects in (a) the rendered color image, which are represented as (b) axis-aligned bounding boxes; the regions are dilated to account for shadows and other defects, and (c) are masked for further completion.

We use a pre-trained VGG16 model (Simonyan and Zisserman, 2014) as the backbone for feature extraction owing to its simplicity. Although existing datasets (Everingham et al., 2010; Lin et al., 2014) already contain training samples for vehicles, they are generally in perspective view rather than orthogonal view from the top. Therefore, we interactively label a small set of datasets for object detection using Labellmg (Tzutalin, 2015). The datasets are exported in Pascal VOC format (Everingham et al., 2010).

We use photogrammetric mesh models covering both the campus of Southwest Jiaotong University (SWJTU) and part of Shenzhen to generate the training samples. The images were obtained using an UAV (unmanned aerial vehicle) and a manned aircraft for SWJTU and Shenzhen, respectively. Typical road areas are selected and rendered from the tiled mesh models. In summary, approximately 250 patches from these two datasets are collected and interactively labeled for training. During training, data augmentation by rotation and mirroring are used for improved generalizability. After the detection of the bounding boxes, each object is enlarged by



approximately 10% to account for shadows and other possible defects in the textured models. The output is a masked raster  $\mathcal{R}_m$ , as shown in Figure 6c.

### 3.4. Extraction of linear regularities

Structured scenes, such as regularly arranged objects, are probably the most challenging cases for image completion (He and Sun, 2012). Unfortunately, scenes of urban roads featuring repeated line markers are highly structured. It is desirable to explicitly consider regularities in the image completion process for improved performance in structured environments (Liu et al., 2010). Therefore, in this study, we first extract two types of linear regularities before the completion of the void regions in the rendered images, that is, translational regularities and linear features.

More specifically, this study adopts the PatchMatch-based (Barnes et al., 2009) approach to complete void regions of vehicles based on Huang et al. (2014). PatchMatch is based on an effective approach to generate the nearest neighbor field (NNF)  $\mathcal{N}$ . Each pixel of the NNF  $\mathbf{v} = \mathcal{N}(\mathbf{p})$  denotes the offset  $\mathbf{v}$  to the correspondence in the same image. The completion is performed by filling the void region with the most self-similar patch. The regularities are injected in this step to guide the generation of the NNF, which not only accelerates the convergence speed but also makes the NNF structure-aware.

*Translational Regularity.* Inspired by previous work (He and Sun, 2012; Huang et al., 2014), we also detect translational regularities using matched image features. However, we found that for urban roads, the offsets between matched features exhibit clear linear regularities. Specifically, we first extract SIFT (Lowe, 2004) features in the rendered image and then obtain matches using the standard ratio check. Unlike in the case of feature matching between two images, no further outlier filtering using random sample consensus (RANSAC) (Fischler and Bolles, 1981) is used.

Three typical results for the feature matches are shown in Figure 7. It should be noted that the offsets of the feature matches exhibit a clear pattern of pointwise and linear clusters. The pointwise clustering center indicates that similar patches are generally located at fixed intervals, such as equal distances between the road markings. On the other hand, the linear pattern indicates that self-similar patches are quite likely to be retrieved by searching along the corresponding direction. In addition, the orthogonal direction is commonly coexistent. Although pointwise clusters are also highly common, in this study, we only enforce linear regularities for two reasons: (1) The point centers are generally aligned along the same line, and (2) as there are an excessive number of point centers, considering all of them significantly affects the efficiency of patch-matching completion (Barnes et al., 2009). In summary, the orientations  $\theta$  detected by RANSAC (Fischler and Bolles, 1981) and the orthogonal directions are then used in structure-aware image completion, that is, a set of  $n$  angles  $\Theta = \{\theta_1, \dots, \theta_n\}$ .



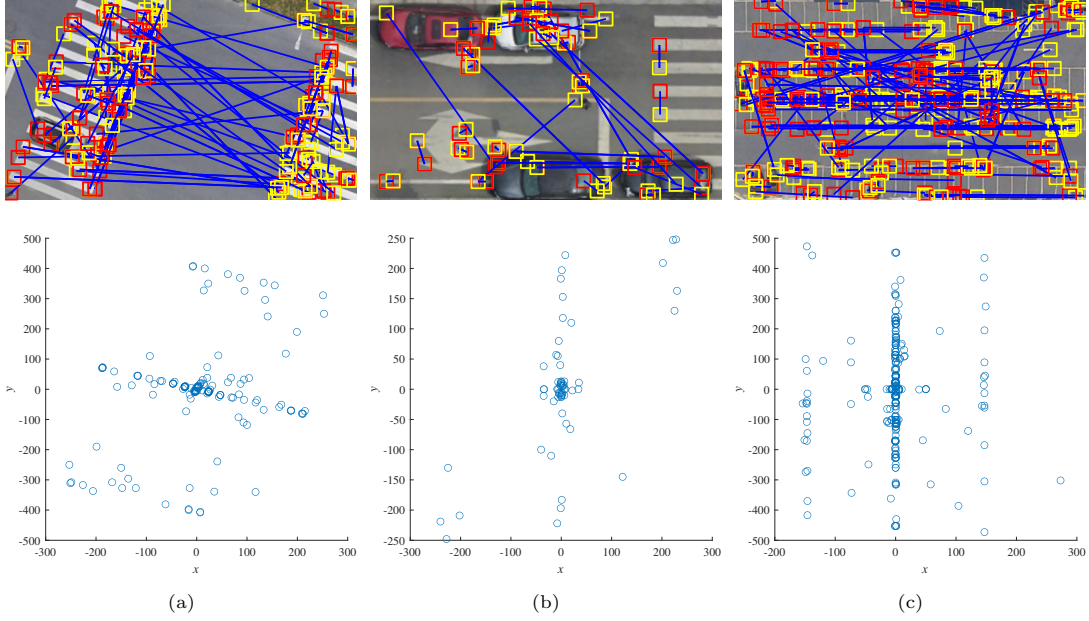


Figure 7: Translational regularities of the matches for three typical scenarios. The top row shows the feature matches of the images to be completed, where the blue lines indicate the offsets of two matched points (red and yellow rectangles). The bottom row shows scatter plots of the offsets for the corresponding match results, which exhibit obvious linear patterns.

*Edge Feature.* Translational regularities are a good indicator of mid-level knowledge for the scenes, and they are used in guided completion. In addition, we directly consider low-level vision features, such as image edges, which also form the skeleton of road scenes. Although there are several choices to detect edge features, such as the line segment detector (LSD) (Von Gioi et al., 2012; Zhu et al., 2020b), we found that LSD and other approaches designed for contour extraction are more sensitive to scene noise (shown in Figure 8). Unfortunately, the rendered image from the textured meshes is inevitably noise-laden owing to defects in the MVS pipeline. Therefore, we directly adopt an efficient gradient filter to extract binary edges  $\mathcal{R}_l$  from the rendered image  $\mathcal{R}_c$ , namely, the Prewitt filter.

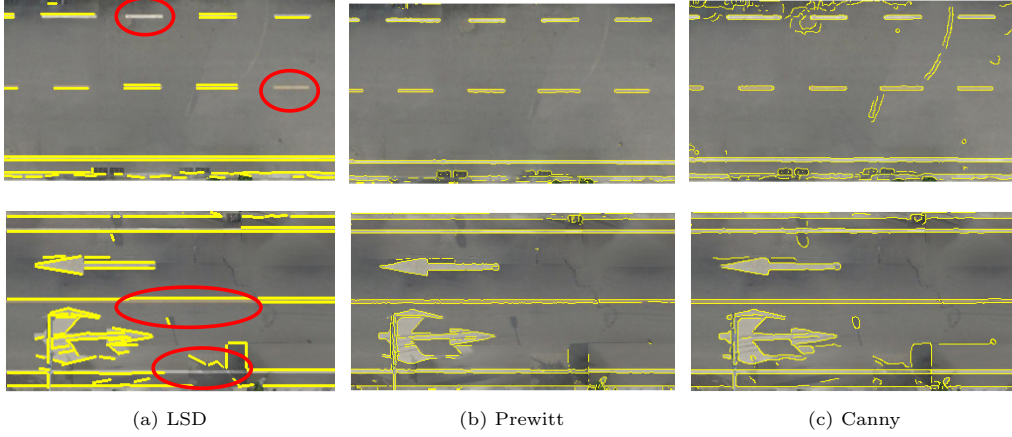


Figure 8: Detected edges by different methods. (a) Lines extracted by LSD. (b) and (c) show the detected edges using Prewitt and Canny operators, respectively.

### 3.5. Structure-aware completion of urban roads

The objective of the completion of urban roads is to recover void regions in  $\mathcal{R}_m$  (Figure 6c) using the orientations  $\Theta$  of translational regularities (Figure 7) and edge maps  $\mathcal{R}_l$ . A pyramid scheme is established based on the PatchMatch strategy (Barnes et al., 2009) to search for the best NNF  $\mathcal{N}$  progressively (Figure 9). Namely, beginning with the coarsest level, a random  $\mathcal{N}$  is initialized, and the edge map  $\mathcal{R}_l$  is generated from the coarsest image mask  $\mathcal{R}_m$ . We first establish a priority queue  $Q$ , which prefers pixels with higher edge scores. The order of the PatchMatch-based expansion is determined by the priority queue  $Q$  rather than the original scanline-based strategy (Barnes et al., 2009). For each pixel  $p$  in  $Q$ , the NNF  $\mathcal{N}(p)$  is refined using an improved updating strategy guided by the linear regularities  $\Theta$ . An example of the progressively refined NNF  $\mathcal{N}$  and completed image  $\mathcal{R}_c$  is shown in Figure 10.

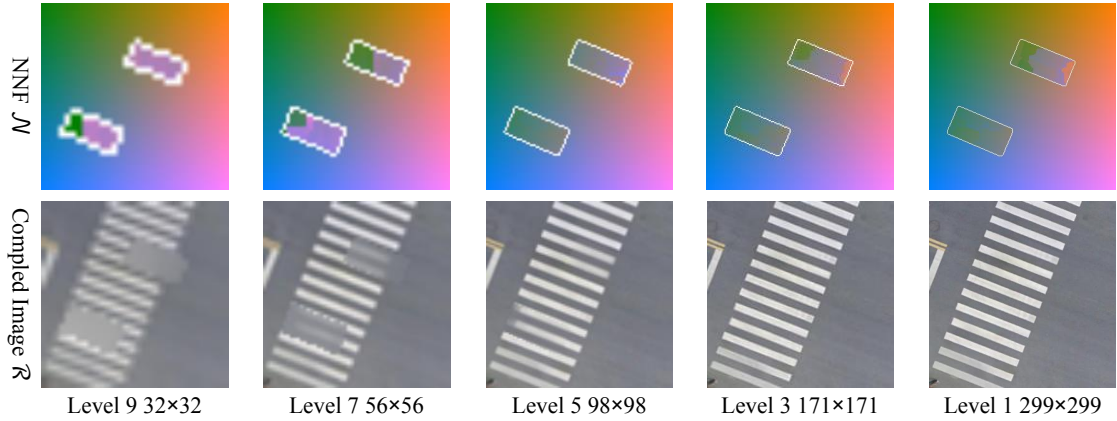


Figure 10: Updated NNF  $\mathcal{N}$  and completed image  $\mathcal{R}_c$  using a pyramid scheme. The white masks in the first row indicate the masked regions.

#### 3.5.1. Generation of priority queue with edge maps

Beginning with a randomly initialized NNF  $\mathcal{N}$ , the vanilla PatchMatch refines  $\mathcal{N}$  in the canonical scanline direction in odd iterations, that is, top to down and left to right, and in the

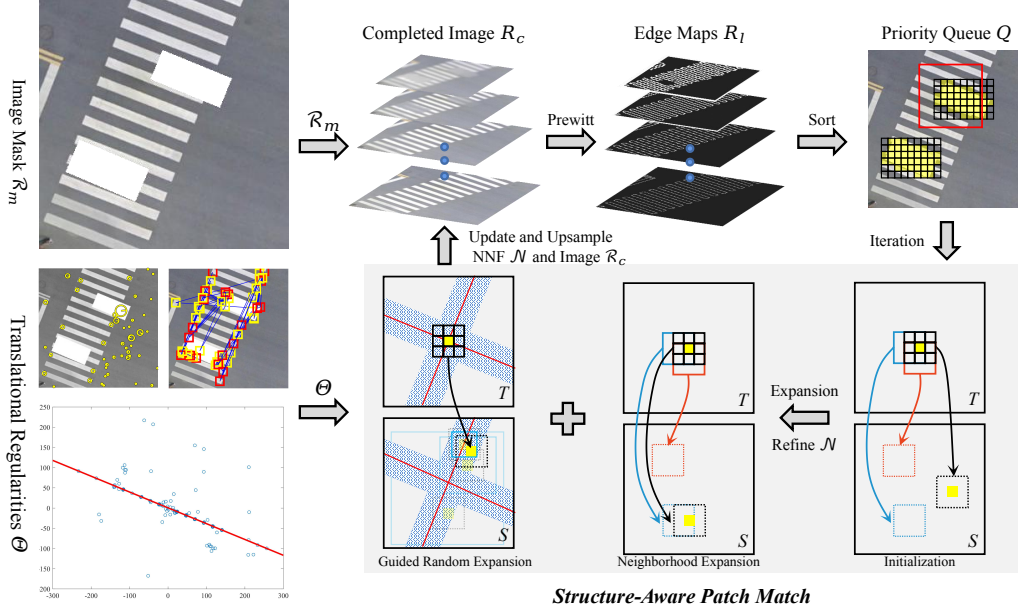


Figure 9: Pyramid scheme for the structure-aware completion of urban roads. A priority queue is generated from the edge maps to prioritize the structured region. In addition, a guided random expansion is considered with translational regularities to retrieve more structured regions. The NNF  $\mathcal{N}$  determines the offset between the most self-similar source  $S$  and the target  $T$  patches.

reverse direction in even iterations (Barnes et al., 2009). However, this may clear artifacts in structured regions. If the patch is expanded from the textureless region to the structured region, the regularity embedded in the structures may not be preserved.

Therefore, we propose an effective approach to remedy this. We argue that structured regions generally have higher edge responses, that is, number of edge pixels in a local patch. Specifically, the sum of the center-aligned square patch on the binary edge map  $\mathcal{R}_l$  is used to represent the responses of the edge. Then, the pixels in the void region are sorted in descending order according to the edge responses in the priority queue  $Q = \{p_1, p_2, \dots, p_n\}$ .

### 3.5.2. Structure-aware similarity measure of patches

To refine the NNF  $\mathcal{N}$ , Barnes et al. (2009) compares the similarity of the current pixel  $p$  with that of its 4-neighborhood with regard to the offset  $v = \mathcal{N}(p)$ . Two square patches are generated as follows:

$$\begin{aligned} T(p) &= \{\mathcal{R}_c(p + s) | s \in [-\frac{W}{2}, \frac{W}{2}] \times [-\frac{W}{2}, \frac{W}{2}]\} \\ S(p, v) &= T(p + v) \end{aligned} \quad (1)$$

where  $T$  and  $S$  are the target and source patches centered around  $p$  and  $p + v$ , respectively. The target patch  $T$  is inside the region to be completed, and the source patch  $S$  is outside the region. It should be noted that during patch expansion, the offset  $v$  may not be sampled from the corresponding pixel  $p$  of NNF  $\mathcal{N}$ ; it can also be sampled from the 4-neighborhood  $N_4(p)$  of  $p$  or even from a random location (Barnes et al., 2009).  $W$  is the patch size, and  $W = 21$  is generally used. The similarity (or matching cost) can be intuitively computed from the grayscale values of the two patches (Barnes et al., 2009). However, we also consider the regularities  $\Theta$  in

the computation of the similarity measure. Specifically, the similarity measure consists of three terms: appearance  $E_a$ , proximity  $E_p$ , and regularity  $E_r$ . That is,

$$E = E_a + \lambda_1 E_p + \lambda_2 E_r \quad (2)$$

where  $\lambda_1 = 5 \times 10^{-4}$  and  $\lambda_2 = 0.5$  are chosen empirically.

1) *Appearance cost*  $E_a(\mathbf{p}, \mathbf{v})$ . We use the sum of the absolute differences between the target and source patches to measure the appearance difference as follows:

$$E_a(\mathbf{p}, \mathbf{v}) = \sum_i w_i |T_i(\mathbf{p}) - T_i(\mathbf{p} + \mathbf{v})| \quad (3)$$

where  $T_i$  and  $S_i$  denote the grayscale values of the  $i$ -th pixel of the patch, and  $w_i$  is an isotropic weight generated from a Gaussian kernel (Huang et al., 2014).

2) *Proximity cost*  $E_p(\mathbf{p}, \mathbf{v})$ . Generally, nearby pixels are preferred over distant pixels (Kopf et al., 2012). Therefore, we add an additional penalty  $E_p$  to prevent selecting distant patches in the NNF  $\mathcal{N}$ , as in (Huang et al., 2014):

$$E_p(\mathbf{p}, \mathbf{v}) = \frac{\|\mathbf{v}\|^2}{\sigma_d(\mathbf{p})^2 + \sigma_c^2} \quad (4)$$

where  $\sigma_d$  and  $\sigma_c$  are normalizers. Specifically,  $\sigma_d(\mathbf{p})$  is the distance to the nearest border of the invalid regions, and  $\sigma_c = \max(w, h)/8$  accounts for the size of image  $(w, h)$ .  $E_p(\mathbf{p})$  prefers small offsets in the NNF  $\mathcal{N}$ .

3) *Regularity cost*  $E_r(\mathbf{v})$ . In structured scenes, the offset direction  $\theta_{\mathbf{v}}$  in the NNF should be consistent with the detected regularities  $\Theta$ . We use the minimum angle difference to measure the regularity cost.

$$E_r(\mathbf{v}) = \min_{\theta \in \Theta} \cos(\theta_{\mathbf{v}} - \theta) \quad (5)$$

### 3.5.3. Guided random expansion

During the expansion of the NNF  $\mathcal{N}$ , PatchMatch (Barnes et al., 2009) tests the similarities of both the 4-Neighborhood  $N_4(\mathbf{p})$  and a set of random pixels centered around  $\mathbf{p}$  as  $R(\mathbf{p}) = \{\mathbf{q}_1, \mathbf{q}_2, \dots, \mathbf{q}_r\}$ . The random set prevents the occurrence of local minima of the expansion. In this study, the directions determined by the translational regularities  $\Theta$  are also used to guide the random expansion, as in the case of the regularity cost. Specifically, the random pixels should be selected in a rectangular buffer along the direction  $\theta \in \Theta$  and the orthogonal direction  $\theta + \frac{\pi}{2}$ , as indicated by the shaded blue region in Figure 9. In addition, a series of  $r$  random pixels with decreasing radius are selected. The radius for pixel  $\mathbf{q}_r$  is determined by  $\max(w, h) \times (\frac{1}{2})^r$ . In summary, a single iteration of the refinement process for the proposed structure-aware PatchMatch is shown in Algorithm 1.

---

**Algorithm 1** Structure-aware PatchMatch.

---

```

procedure PATCHMATCH( $\mathcal{N}, \mathcal{R}_c, Q, R$ )
2:   for  $p \in Q$  do
      for  $q \in N_4(p)$  do                                     ▷ Neighborhood Expansion
4:       if  $E(p, \mathcal{N}(q)) < E(p, \mathcal{N}(p))$  then
            $\mathcal{N}(p) \leftarrow \mathcal{N}(q)$ 
6:       end if
      end for
8:       for  $q \in R(p)$  do                                     ▷ Guided Random Expansion
           if  $E(p, \mathcal{N}(q)) < E(p, \mathcal{N}(p))$  then
10:             $\mathcal{N}(p) \leftarrow \mathcal{N}(q)$ 
           end if
12:      end for
      end for
14:   return  $\mathcal{N}$ 
end procedure
```

---

#### 4. Experimental evaluation and analysis

##### 4.1. Dataset description

To evaluate the proposed methods, we use three datasets, which consist of highways, parking lots, and roads with and without marker lines (Figure 11). The first was collected from the campus of Southwest Jiaotong University (SWJTU) in Chengdu, China. Two typical regions are considered, including a road with no parking signs and a cross intersection. The second was collected from a block in Shenzhen of China. We select an alley with numerous vehicles parked and a residential area for the experiments. The third was provided by courtesy of ISPRS in Dortmund, Germany (Nex et al., 2015). The road areas on a bridge and a park lot on a building roof were selected for the experiments.

In addition to the different road scenarios, the three datasets were also captured by different sensors at different relative flight heights on different platforms. Table 1 lists the type of sensor, relative flight height, ground sample distance (GSD), and the number of images for the three datasets. It should be also noted that the SWJTU dataset was captured by a UAV, and the other two by a manned aircraft.

Table 1: Detailed description of the datasets

Dataset	SWJTU	Shenzhen	Dortmund
Sensor	SONY ICLE-5100	PHASE ONE IQ180	IGI PentaCam
Relative flight height (m)	85.23	918.66	831.97
Ground sample distance (cm)	1.6-2.0	6.0-8.0	8.0-12.0

##### 4.2. Results

###### 4.2.1. Texture integration

To resolve the issue caused by the discontinuous texture image, we first integrate the texels in different charts into a unified image through orthogonal rendering of the textured mesh models. Figure 12 shows the integrated image for the three datasets. The red rectangle in the top-left part of each subfigure is interactively selected by the operator, and only the triangles inside the



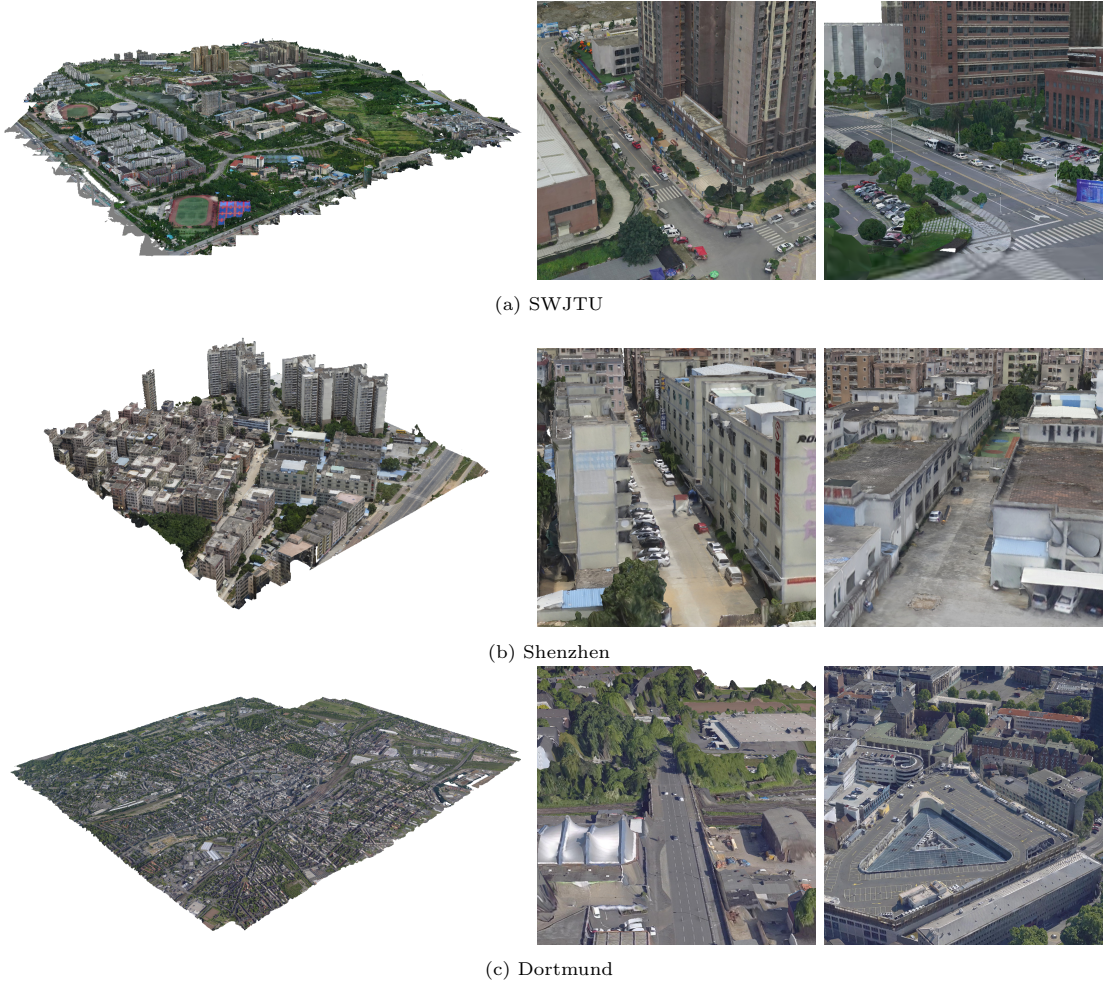


Figure 11: Datasets used for the experimental evaluations. Different road scenarios are considered. In addition, the three datasets were captured by different sensors at different ground resolutions.

selected ROI are considered for further processing. The yellow highlighted regions in the bottom-left part of each subfigure indicate the facets involved in the UV mesh. Even though the ROI only accounts for a small rectangular area, several small charts are involved; direct processing is difficult owing to the fragments in the UV mesh. This is resolved through efficient rendering of the mesh models (Figure 12, right part). The resolution of the viewport is selected according to the average GSD of the model; this ensures that the texture information is preserved during the rendering process.



Figure 12: Integration of the texture by orthogonal rendering of the mesh models. The red rectangle in the top-left of each subfigure is the selected ROI in the mesh model. The yellow highlight in the bottom-left part indicates the corresponding facets selected on the UV mesh. The right part of each subfigure shows the rendered image.

#### 4.2.2. Image and mesh completion

After obtaining the rendered image  $\mathcal{R}_c$ , we directly detect the vehicles using Faster R-CNN (Ren et al., 2015), from which the mask image  $\mathcal{R}_m$  is obtained. Then, the void regions are completed using the proposed methods as  $\mathcal{R}'_c$  and deintegrated to mesh texture. In addition, we flatten the triangles inside the masked regions for the completed mesh  $\mathcal{M}'$ .

Figures 13 to 15 show the completed results for both the images and mesh models. Two regions for each dataset are separated into the top and bottom halves. Except for the shadow regions in the Dortmund dataset, the results are quite satisfactory. The road markers are recovered reasonably well, such as the crosswalk and X-cross in the SWJTU dataset, and the structured labels in the parking lot of the Dortmund dataset. For the Shenzhen dataset, the faint structure patterns on the textureless road are also preserved. The right part of each figure shows the mesh models before and after completion from four different viewpoints. The proposed methods can produce cleaner road scenes after flattening the geometries and completing the textures of the mesh models. More supplementary video demonstrations involving large regions are available at <https://vrlab.org.cn/~hanhu/projects/mesh>.



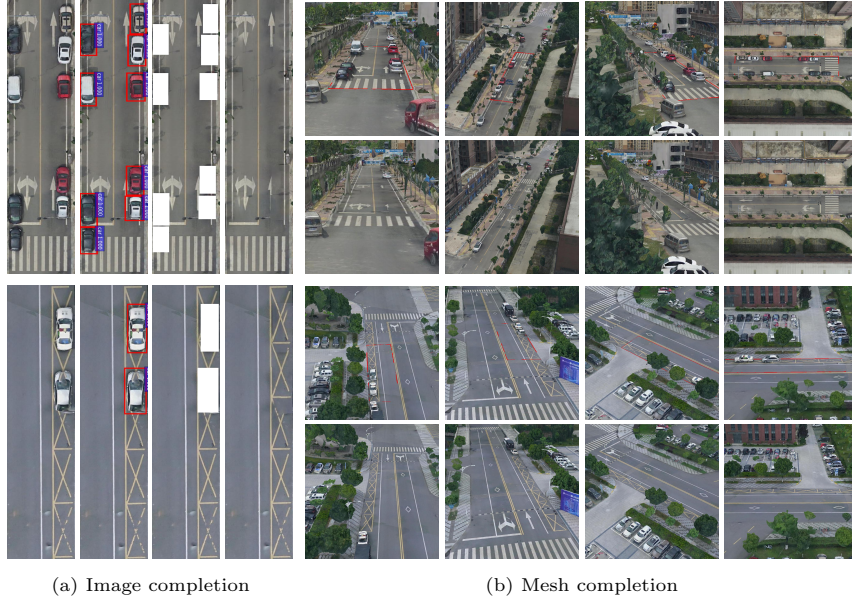


Figure 13: Completed mesh models for the two regions of the SWJTU dataset. (a) Completion of images; the four columns show the rendered image  $\mathcal{R}_c$ , indicated bounding boxes, masked image  $\mathcal{R}_m$ , and completed image  $\mathcal{R}'_c$ . (b) Completed mesh models; the top and bottom rows for each region show the original models  $\mathcal{M}$  and completed models  $\mathcal{M}'$ , respectively.

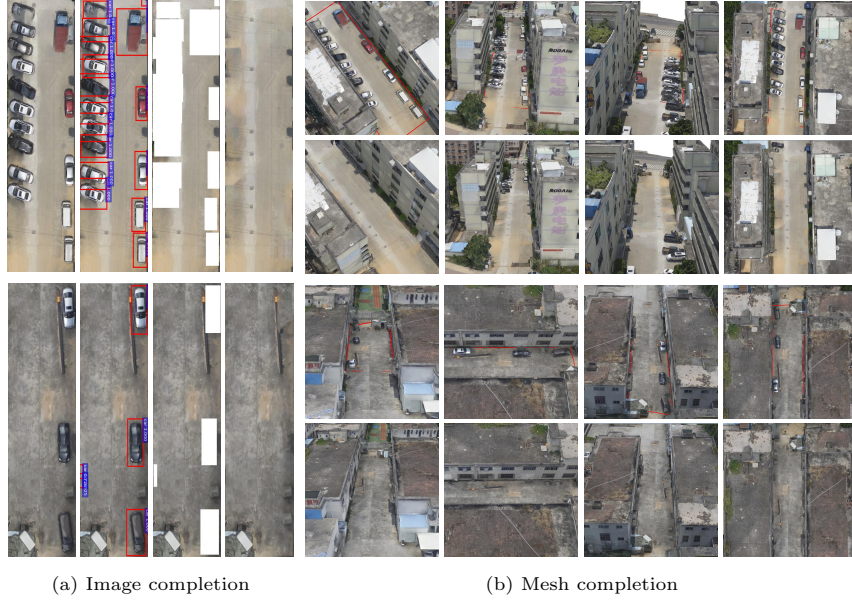


Figure 14: Completed mesh models for the two regions of the Shenzhen dataset. (a) Completion of images; the four columns show the rendered image  $\mathcal{R}_c$ , indicated bounding boxes, masked image  $\mathcal{R}_m$ , and completed image  $\mathcal{R}'_c$ . (b) Completed mesh models; the top and bottom rows for each region show the original models  $\mathcal{M}$  and completed models  $\mathcal{M}'$ , respectively.

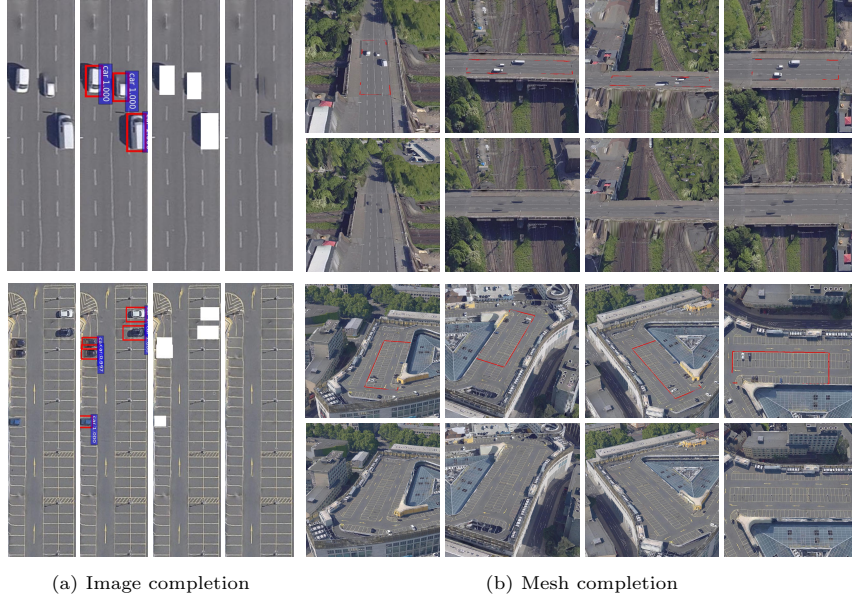


Figure 15: Completed mesh models for the two regions of the Dortmund dataset. (a) Completion of images; the four columns show the rendered image  $\mathcal{R}_c$ , indicated bounding boxes, masked image  $\mathcal{R}_m$ , and completed image  $\mathcal{R}'_c$ . (b) Completed mesh models; the top and bottom rows for each region show the original models  $\mathcal{M}$  and completed models  $\mathcal{M}'$ , respectively.

### 4.3. Comparison of image completion

#### 4.3.1. Qualitative comparison

To evaluate the performance of image completion against state-of-the-art approaches, two approaches are considered: methods based on statistics of patch offsets (He and Sun, 2012), and planar structure guidance (Huang et al., 2014). Figures 16 to 18 show the image completion results of the algorithms mentioned above. The first column shows images to be completed; the second column shows reference results edited manually using Adobe Photoshop (Adobe, 2020). Zoomed regions are also shown to provide details of the completion results.

By comparing the results on different datasets, it can be seen that the results by He and Sun (2012) exhibit artificial noise, particularly the result under the simplest scenario in Shenzhen. In addition, although the method in Huang et al. (2014) yields better results than that in He and Sun (2012), blurry areas occur, and perfect linear features cannot be preserved in some experiments. The proposed method exhibits better performance than the other two methods. Specifically, distinct linear features are preserved to achieve desirable completion results, as for example, the zebra crossing and parking lines.

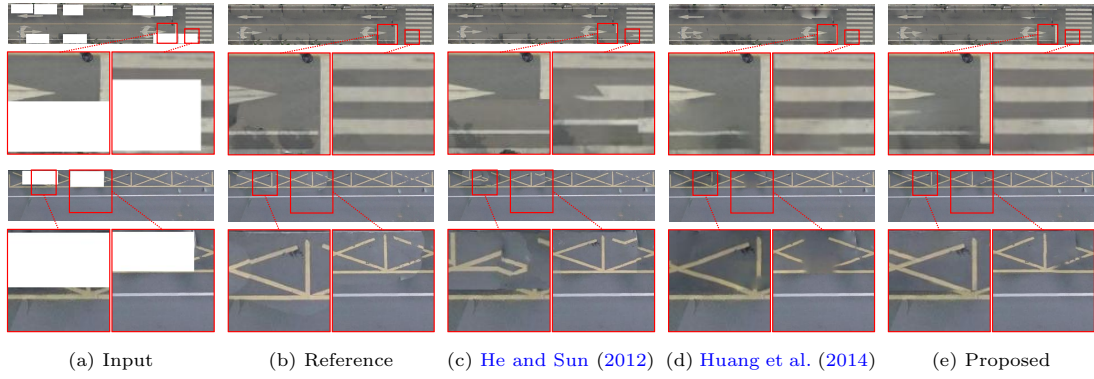


Figure 16: Comparisons of different completion methods on the SWJTU dataset. The red rectangles indicate enlarged regions.

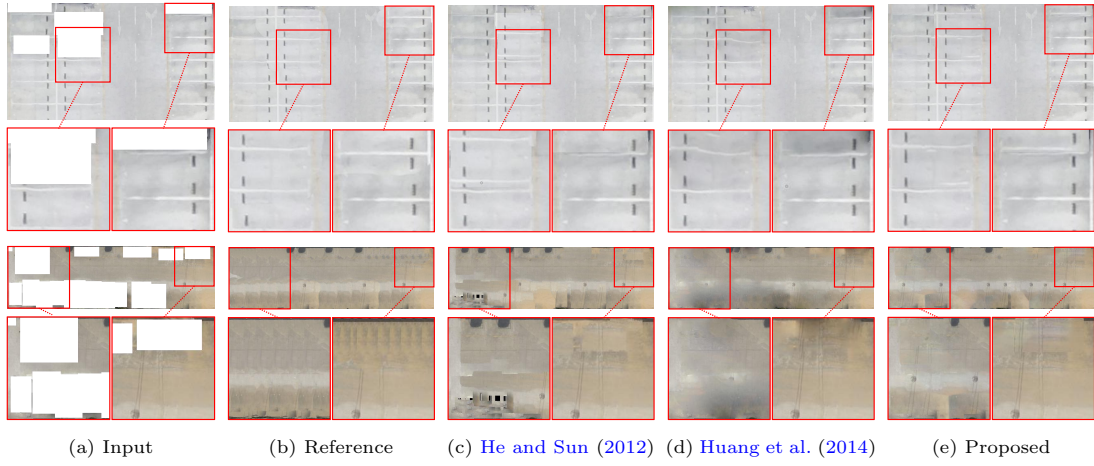


Figure 17: Comparisons of different completion methods on the SWJTU dataset. The red rectangles indicate enlarged regions.



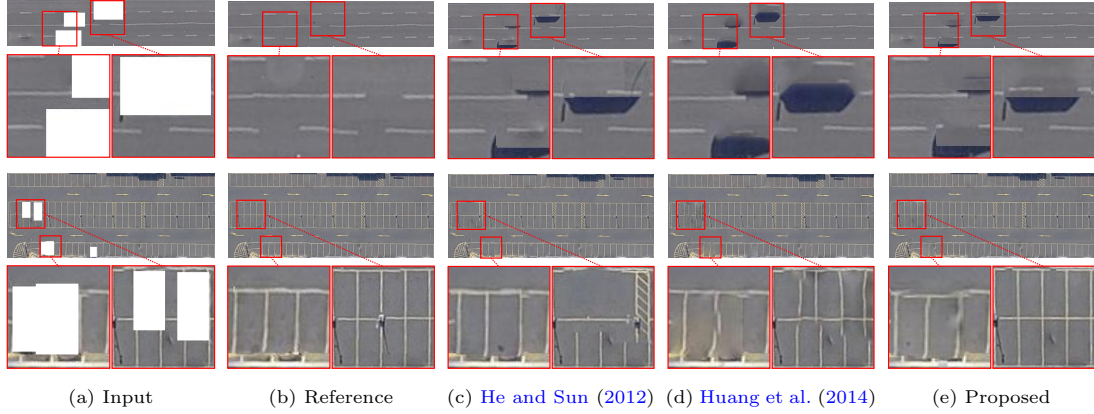


Figure 18: Comparisons of different completion methods on the SWJTU dataset. The red rectangles indicate enlarged regions.

#### 4.3.2. Quantitative comparison

The peak signal-to-noise ratio (PSNR) is the most common and widely used objective evaluation index for images. Structural similarity (SSIM) is another image quality evaluation index. It measures image similarity in terms of brightness, contrast, and structure. Herein, we evaluate the completion results on road area texture integration images in terms of PSNR and SSIM, as in (Hore and Ziou, 2010). We consider a manually repaired image using Adobe Photoshop as a reference to calculate the PSNR and SSIM of different methods. Table 2 shows these evaluation indexes (Hore and Ziou, 2010). It can be seen that the proposed method has better average PSNR and SSIM than the other two state-of-the-art methods. Regarding PSNR, the proposed method achieved the best results for all the testing samples; regarding SSIM, it achieved the best results for four out of six samples.

Table 2: Comparison with other approaches in terms of PSNR and SSIM on the six datasets. The best results are highlighted in bold.

Dataset		SWJTU1	SWJTU2	Shenzhen1	Shenzhen2	Dortmund1	Dortmund2	Average
PSNR	Proposed method	<b>27.49</b>	<b>25.40</b>	<b>26.56</b>	<b>24.98</b>	<b>29.67</b>	<b>33.88</b>	<b>28.00</b>
	He and Sun (2012)	26.92	25.30	26.20	23.16	29.45	32.94	27.33
	Huang et al. (2014)	25.38	24.51	22.54	22.84	27.09	32.42	25.80
SSIM	Proposed method	<b>0.932</b>	<b>0.888</b>	0.918	<b>0.894</b>	0.950	<b>0.975</b>	<b>0.926</b>
	He and Sun (2012)	0.919	0.878	<b>0.926</b>	0.883	<b>0.954</b>	0.969	0.921
	Huang et al. (2014)	0.925	0.882	0.920	0.866	0.947	0.954	0.916

#### 4.4. Analysis of linear guidance and directional constraint

The proposed method prioritizes the target patches and constrains the random searching area to improve the completion result. To evaluate the effect of the priority setting by linear guidance and directionally constrained searching, we conducted ablation studies. Figure 19 shows typical comparisons between methods under different settings.

Table 3: Completion results evaluation under different algorithm settings. The best results are highlighted in bold.

Evaluation	Method	SWJTU1	SWJTU2	Shenzhen1	Shenzhen2	Dortmund1	Dortmund2
PSNR	Proposed	<b>27.27</b>	<b>25.67</b>	<b>25.24</b>	<b>28.96</b>	28.36	<b>34.11</b>
	w/o. Directional Guidance	26.41	24.67	25.03	28.77	<b>28.49</b>	32.28
	w/o. Linear Ordering	26.53	24.86	25.10	28.55	28.48	32.33
	w/o. Both	26.15	25.00	24.94	28.45	28.48	34.07
SSIM	Proposed	<b>0.930</b>	<b>0.893</b>	0.901	<b>0.944</b>	0.935	<b>0.976</b>
	w/o. Directional Guidance	0.912	0.880	0.899	<b>0.944</b>	0.945	0.966
	w/o. Linear Ordering	0.915	0.876	<b>0.902</b>	0.941	0.945	0.966
	w/o. Both	0.910	0.878	0.900	0.942	<b>0.947</b>	0.975

By comparing the results in Figure 19, it can be concluded that the two strategies remarkably improve the completion results in complex scenarios with numerous linear structures. In addition, these methods yield similar results in a simple scenario, for example, Shenzhen1. From Table 3, it can be seen, that except for Shenzhen1 and Dortmund1, the proposed method yields the best completion results. The failure of the proposed method in these datasets can be attributed to the fact that both datasets have few artificial linear structures. In fact, it is also demonstrated that the guidance of a linear feature is valid in image completion of urban road areas, which always have numerous linear features.

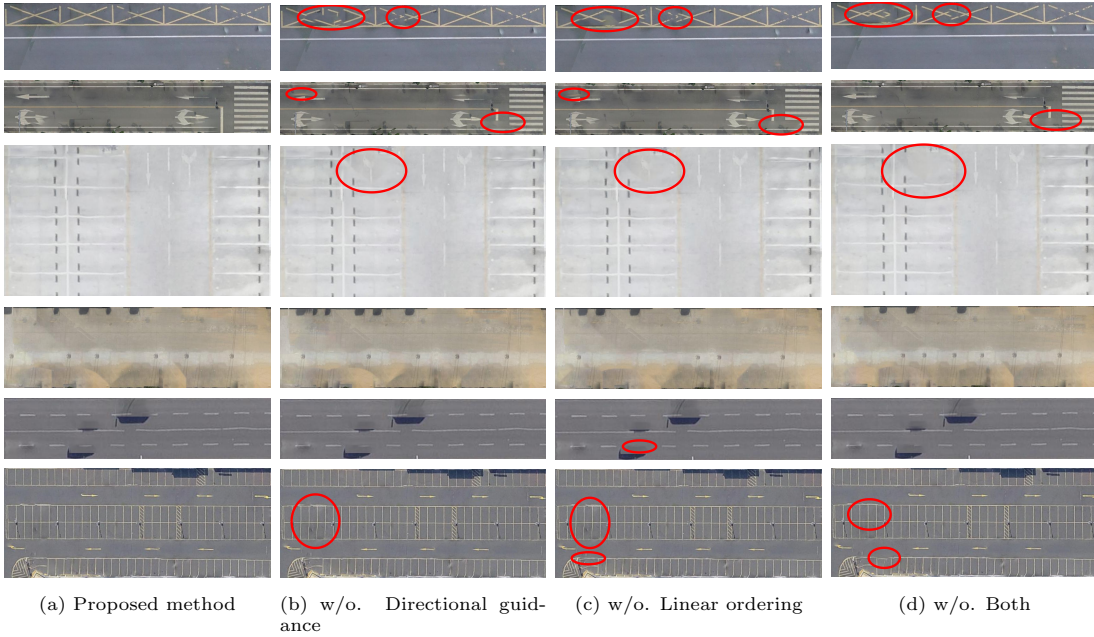


Figure 19: Completion results under different settings. Highlighted regions are where the errors appear.

#### 4.5. Discussion and limitations

It can intuitively be seen that the proposed mesh completion method yields superior results, which are difficult to obtain by using UV editing tools in modeling software. After completion, regions with no useful texture image, for example, regions occluded by cars, can obtain a plausible texture. The quantitative experiments demonstrate that synthetic texture is sufficient as a model exhibition. Moreover, the proposed structure-aware image completion algorithm can achieve effects similar to those by traditional manual repair methods using Photoshop, with little

interaction and higher automation. It is also more effective than state-of-the-art methods (He and Sun, 2012; Huang et al., 2014) in image completion of urban roads.

Despite the good completion results, there are certain limitations. First, the proposed image completion algorithm is not always stable because of the random search. However, we improved it compared with state-of-the-art methods (Barnes et al., 2009; Huang et al., 2014). Second, when blank regions have no connection with the surrounding pixels, the proposed completion algorithm cannot be applied. In the future, we will conduct related research on texture generation in semantic models.

## 5. CONCLUSION

In this paper, we presented a road-area oblique photogrammetry 3D model completion method with few interactions. It can remove undesirable vehicles and retain a reasonable geometry structure and texture appearance, particularly artificial repetitive structures. Traditional methods cannot efficiently edit 3D models with discrete textures. We also proposed a texture editing method. In addition, a structure-aware image completion algorithm with superior performance on road area images was proposed for automatic texture completion. After experimental evaluation and analysis, the advantages and limitations of the proposed method were demonstrated.

## Acknowledgments

This work was supported in part by the National Key Research and Development Program of China (Project No. 2018YFC0825803) and by the National Natural Science Foundation of China (Project No. 41631174, 42071355, 41871291). In addition, the authors gratefully acknowledge the provision of the datasets by ISPRS and EuroSDR, which were released in conjunction with the ISPRS Scientific Initiatives 2014 and 2015, led by ISPRS ICWG I/Vb.

## References

- Adobe, 2020. Adobe photoshop. <https://www.adobe.com/cn/products/photoshop.html>.
- Agarwala, A., 2007. Efficient gradient-domain compositing using quadrees. *ACM Transactions on Graphics (TOG)* 26, 94–es.
- Allène, C., Pons, J.P., Keriven, R., 2008. Seamless image-based texture atlases using multi-band blending, in: 2008 19th International Conference on Pattern Recognition, IEEE. pp. 1–4.
- Aubert, G., Kornprobst, P., 2006. Mathematical problems in image processing: partial differential equations and the calculus of variations. volume 147. Springer Science & Business Media.
- Barnes, C., Shechtman, E., Finkelstein, A., Goldman, D.B., 2009. Patchmatch: A randomized correspondence algorithm for structural image editing, in: *ACM Transactions on Graphics (ToG)*, ACM. p. 24.
- Bertalmio, M., Sapiro, G., Caselles, V., Ballester, C., 2000. Image inpainting, in: *Proceedings of the 27th annual conference on Computer graphics and interactive techniques*, pp. 417–424.
- Bi, S., Kalantari, N.K., Ramamoorthi, R., 2017. Patch-based optimization for image-based texture mapping. *ACM Trans. Graph.* 36, 106–1.

- Chen, Z., Liu, C., Wu, H., 2019. A higher-order tensor voting-based approach for road junction detection and delineation from airborne lidar data. *ISPRS journal of photogrammetry and remote sensing* 150, 91–114.
- Cohen-Steiner, D., Alliez, P., Desbrun, M., 2004. Variational shape approximation, in: *ACM SIGGRAPH 2004 Papers*, pp. 905–914.
- Crane, K., de Goes, F., Desbrun, M., Schröder, P., 2013. Digital geometry processing with discrete exterior calculus, in: *ACM SIGGRAPH 2013 courses*, ACM, New York, NY, USA.
- Criminisi, A., Pérez, P., Toyama, K., 2004. Region filling and object removal by exemplar-based image inpainting. *IEEE Transactions on image processing* 13, 1200–1212.
- Dalal, N., Triggs, B., 2005. Histograms of oriented gradients for human detection, in: *2005 IEEE computer society conference on computer vision and pattern recognition (CVPR’05)*, IEEE. pp. 886–893.
- Everingham, M., Van Gool, L., Williams, C.K., Winn, J., Zisserman, A., 2010. The pascal visual object classes (voc) challenge. *International journal of computer vision* 88, 303–338.
- Felzenszwalb, P.F., Girshick, R.B., McAllester, D., Ramanan, D., 2009. Object detection with discriminatively trained part-based models. *IEEE transactions on pattern analysis and machine intelligence* 32, 1627–1645.
- Fischler, M.A., Bolles, R.C., 1981. Random sample consensus: a paradigm for model fitting with applications to image analysis and automated cartography. *Communications of the ACM* 24, 381–395.
- Girshick, R., 2015. Fast r-cnn, in: *Proceedings of the IEEE international conference on computer vision*, pp. 1440–1448.
- Girshick, R., Donahue, J., Darrell, T., Malik, J., 2014. Rich feature hierarchies for accurate object detection and semantic segmentation, in: *Proceedings of the IEEE conference on computer vision and pattern recognition*, pp. 580–587.
- GLM, 2019. OpenGL mathematics. <https://glm.g-truc.net/>.
- Google, 2020. Google earth. <https://www.google.com/earth/>.
- Graves, A., 2013. Generating sequences with recurrent neural networks. *arXiv preprint arXiv:1308.0850*.
- Haala, N., Kada, M., 2010. An update on automatic 3d building reconstruction. *ISPRS Journal of Photogrammetry and Remote Sensing* 65, 570–580.
- He, K., Sun, J., 2012. Statistics of patch offsets for image completion, in: *European Conference on Computer Vision*, Springer. pp. 16–29.
- Hirschmuller, H., 2008. Stereo processing by semiglobal matching and mutual information. *IEEE Transactions on pattern analysis and machine intelligence* 30, 328–341.
- Hore, A., Ziou, D., 2010. Image quality metrics: Psnr vs. ssim, in: *2010 20th International Conference on Pattern Recognition*, IEEE. pp. 2366–2369.

- Hu, H., Chen, C., Wu, B., Yang, X., Zhu, Q., Ding, Y., 2016a. Texture-aware dense image matching using ternary census transform. *ISPRS annals of the photogrammetry, remote sensing and spatial information sciences* .
- Hu, H., Ding, Y., Zhu, Q., Wu, B., Xie, L., Chen, M., 2016b. Stable least-squares matching for oblique images using bound constrained optimization and a robust loss function. *ISPRS journal of photogrammetry and remote sensing* 118, 53–67.
- Hu, H., Wu, B., Chen, L., 2019. Color balancing and geometrical registration of high-resolution planetary imagery for improved orthographic image mosaicking. *Planetary and Space Science* 178, 104719.
- Hu, H., Zhu, Q., Du, Z., Zhang, Y., Ding, Y., 2015. Reliable spatial relationship constrained feature point matching of oblique aerial images. *Photogrammetric Engineering & Remote Sensing* 81, 49–58.
- Huang, J.B., Kang, S.B., Ahuja, N., Kopf, J., 2014. Image completion using planar structure guidance. *ACM Transactions on graphics (TOG)* 33, 1–10.
- Iizuka, S., Simo-Serra, E., Ishikawa, H., 2017. Globally and locally consistent image completion. *ACM Transactions on Graphics (ToG)* 36, 1–14.
- Isenburg, M., 2020. Open data. <https://rapidlasso.com/category/open-data/>.
- Jancosek, M., Pajdla, T., 2011. Multi-view reconstruction preserving weakly-supported surfaces, in: *CVPR 2011, IEEE*. pp. 3121–3128.
- Kada, M., McKinley, L., 2009. 3d building reconstruction from lidar based on a cell decomposition approach. *International Archives of Photogrammetry, Remote Sensing and Spatial Information Sciences* 38, W4.
- Kazhdan, M., Hoppe, H., 2013. Screened poisson surface reconstruction. *ACM Transactions on Graphics (ToG)* 32, 1–13.
- Kazhdan, M., Surendran, D., Hoppe, H., 2010. Distributed gradient-domain processing of planar and spherical images. *ACM Transactions on Graphics (TOG)* 29, 1–11.
- Kopf, J., Kienzle, W., Drucker, S., Kang, S.B., 2012. Quality prediction for image completion. *ACM Transactions on Graphics (TOG)* 31, 1–8.
- Lévy, B., Petitjean, S., Ray, N., Maillot, J., 2002. Least squares conformal maps for automatic texture atlas generation. *ACM transactions on graphics (TOG)* 21, 362–371.
- Limper, M., Vining, N., Sheffer, A., 2018. Box cutter: atlas refinement for efficient packing via void elimination. *ACM Trans. Graph.* 37, 153–1.
- Lin, T.Y., Maire, M., Belongie, S., Hays, J., Perona, P., Ramanan, D., Dollár, P., Zitnick, C.L., 2014. Microsoft coco: Common objects in context, in: *European conference on computer vision*, Springer. pp. 740–755.
- Liu, H.Y., Fu, X.M., Ye, C., Chai, S., Liu, L., 2019. Atlas refinement with bounded packing efficiency. *ACM Transactions on Graphics (TOG)* 38, 1–13.
- Liu, S., Ferguson, Z., Jacobson, A., Gingold, Y.I., 2017. Seamless: seam erasure and seam-aware decoupling of shape from mesh resolution. *ACM Trans. Graph.* 36, 216–1.



- Liu, W., Anguelov, D., Erhan, D., Szegedy, C., Reed, S., Fu, C.Y., Berg, A.C., 2016. Ssd: Single shot multibox detector, in: European conference on computer vision, Springer. pp. 21–37.
- Liu, Y., Hel-Or, H., Kaplan, C.S., Van Gool, L., et al., 2010. Computational symmetry in computer vision and computer graphics. *Foundations and Trends® in Computer Graphics and Vision* 5, 1–195.
- Lowe, D.G., 2004. Distinctive image features from scale-invariant keypoints. *International journal of computer vision* 60, 91–110.
- Nazeri, K., Ng, E., Joseph, T., Qureshi, F.Z., Ebrahimi, M., 2019. Edgeconnect: Generative image inpainting with adversarial edge learning. *arXiv preprint arXiv:1901.00212*.
- Nex, F., Gerke, M., 2014. Photogrammetric dsm denoising. *The International Archives of Photogrammetry, Remote Sensing and Spatial Information Sciences* 40, 231.
- Nex, F., Remondino, F., Gerke, M., Przybilla, H.J., Bäumker, M., Zurhorst, A., 2015. Isprs benchmark for multi-platform photogrammetry. *ISPRS Annals of Photogrammetry, Remote Sensing & Spatial Information Sciences* 2.
- Ojala, T., Pietikainen, M., Maenpää, T., 2002. Multiresolution gray-scale and rotation invariant texture classification with local binary patterns. *IEEE Transactions on pattern analysis and machine intelligence* 24, 971–987.
- Papageorgiou, C.P., Oren, M., Poggio, T., 1998. A general framework for object detection, in: *Sixth International Conference on Computer Vision (IEEE Cat. No. 98CH36271)*, IEEE. pp. 555–562.
- Prada, F., Kazhdan, M., Chuang, M., Hoppe, H., 2018. Gradient-domain processing within a texture atlas. *ACM Transactions on Graphics (TOG)* 37, 1–14.
- Redmon, J., Divvala, S., Girshick, R., Farhadi, A., 2016. You only look once: Unified, real-time object detection, in: *Proceedings of the IEEE conference on computer vision and pattern recognition*, pp. 779–788.
- Redmon, J., Farhadi, A., 2017. Yolo9000: better, faster, stronger, in: *Proceedings of the IEEE conference on computer vision and pattern recognition*, pp. 7263–7271.
- Redmon, J., Farhadi, A., 2018. Yolov3: An incremental improvement. *arXiv preprint arXiv:1804.02767*.
- Remondino, F., Gerke, M., 2015. Oblique aerial imagery—a review, in: *Photogrammetric week*, pp. 75–81.
- Remondino, F., Nocerino, E., Toschi, I., Menna, F., 2017. A critical review of automated photogrammetric processing of large datasets. *International Archives of the Photogrammetry, Remote Sensing & Spatial Information Sciences* 42.
- Ren, S., He, K., Girshick, R., Sun, J., 2015. Faster r-cnn: Towards real-time object detection with region proposal networks, in: *Advances in neural information processing systems*, pp. 91–99.
- Schonberger, J.L., Frahm, J.M., 2016. Structure-from-motion revisited, in: *Proceedings of the IEEE Conference on Computer Vision and Pattern Recognition*, pp. 4104–4113.

- Shen, J., Chan, T.F., 2002. Mathematical models for local nontexture inpaintings. *SIAM Journal on Applied Mathematics* 62, 1019–1043.
- Simonyan, K., Zisserman, A., 2014. Very deep convolutional networks for large-scale image recognition. *arXiv preprint arXiv:1409.1556*.
- Sorkine, O., Cohen-Or, D., Goldenthal, R., Lischinski, D., 2002. Bounded-distortion piecewise mesh parameterization, in: *IEEE Visualization, 2002. VIS 2002.*, IEEE. pp. 355–362.
- Sugarbaker, L., Constance, E.W., Heidemann, H.K., Jason, A.L., Lucas, V., Saghy, D., Stoker, J.M., 2014. The 3D Elevation Program initiative: a call for action. *US Geological Survey*.
- Tzutalin, 2015. Labelimg. [github.com/tzutalin/labelImg](https://github.com/tzutalin/labelImg).
- Uijlings, J.R., Van De Sande, K.E., Gevers, T., Smeulders, A.W., 2013. Selective search for object recognition. *International journal of computer vision* 104, 154–171.
- Verdie, Y., Lafarge, F., Alliez, P., 2015. Lod generation for urban scenes. *ACM Transactions on Graphics* 34, 30.
- Verykokou, S., Ioannidis, C., 2018. Oblique aerial images: a review focusing on georeferencing procedures. *International Journal of Remote Sensing* 39, 3452–3496.
- Viola, P., Jones, M.J., 2004. Robust real-time face detection. *International journal of computer vision* 57, 137–154.
- Von Gioi, R.G., Jakubowicz, J., Morel, J.M., Randall, G., 2012. Lsd: a line segment detector. *Image Processing On Line* 2, 35–55.
- Vu, H.H., Keriven, R., Labatut, P., Pons, J.P., 2009. Towards high-resolution large-scale multi-view stereo, in: *2009 IEEE Conference on Computer Vision and Pattern Recognition, IEEE*. pp. 1430–1437.
- Waechter, M., Moehrle, N., Goesele, M., 2014. Let there be color! large-scale texturing of 3d reconstructions, in: *European conference on computer vision, Springer*. pp. 836–850.
- Wenzel, S., Bulatov, D., 2019. Simultaneous chain-forming and generalization of road networks. *Photogrammetric Engineering & Remote Sensing* 85, 19–28.
- Wolfram, 2020. Trilinear coordinates. <https://mathworld.wolfram.com/TrilinearCoordinates.html>.
- Wong, A., Orchard, J., 2008. A nonlocal-means approach to exemplar-based inpainting, in: *2008 15th IEEE International Conference on Image Processing, IEEE*. pp. 2600–2603.
- Wu, X., Xu, K., Hall, P., 2017. A survey of image synthesis and editing with generative adversarial networks. *Tsinghua Science and Technology* 22, 660–674.
- Yang, B., Dong, Z., Liu, Y., Liang, F., Wang, Y., 2017. Computing multiple aggregation levels and contextual features for road facilities recognition using mobile laser scanning data. *ISPRS Journal of Photogrammetry and Remote Sensing* 126, 180–194.
- Yeh, R.A., Chen, C., Yian Lim, T., Schwing, A.G., Hasegawa-Johnson, M., Do, M.N., 2017. Semantic image inpainting with deep generative models, in: *Proceedings of the IEEE conference on computer vision and pattern recognition*, pp. 5485–5493.

- Yu, J., Lin, Z., Yang, J., Shen, X., Lu, X., Huang, T.S., 2018. Generative image inpainting with contextual attention, in: Proceedings of the IEEE conference on computer vision and pattern recognition, pp. 5505–5514.
- Yu, L., Zhang, Y., Sun, M., Zhou, X., Liu, C., 2017. An auto-adapting global-to-local color balancing method for optical imagery mosaic. *ISPRS Journal of Photogrammetry and Remote Sensing* 132, 1–19.
- Yuksel, C., Lefebvre, S., Tarini, M., 2019. Rethinking texture mapping, in: Computer Graphics Forum, Wiley Online Library. pp. 535–551.
- Zhang, C., Xu, M.F., Chai, S., Fu, X.M., 2020. Robust atlas generation via angle-based segmentation. *Computer Aided Geometric Design* , 101854.
- Zhou, Q.Y., Koltun, V., 2014. Color map optimization for 3d reconstruction with consumer depth cameras. *ACM Transactions on Graphics (TOG)* 33, 1–10.
- Zhu, Q., Wang, Z., Hu, H., Xie, L., Ge, X., Zhang, Y., 2020a. Leveraging photogrammetric mesh models for aerial-ground feature point matching toward integrated 3d reconstruction. *ISPRS Journal of Photogrammetry and Remote Sensing* 166, 26–40.
- Zhu, Q., Zhang, M., Hu, H., Wang, F., 2020b. Interactive correction of a distorted street-view panorama for efficient 3-d façade modeling. *IEEE Geoscience and Remote Sensing Letters* .